

1 **Tropopause Evolution in a Rapidly Intensifying Tropical Cyclone: A Static**
2 **Stability Budget Analysis**

3 Patrick Duran* and John Molinari

4 *University at Albany, State University of New York, Albany, NY*

5 **Corresponding author address:* Department of Atmospheric and Environmental Sciences, Univer-
6 sity at Albany, State University of New York, 1400 Washington Avenue, Albany, NY.

7 E-mail: pduran2008@gmail.com

ABSTRACT

⁸ We have some cool results!

9 **1. Introduction**

10 There will be a whole bunch of papers cited here...

11 **2. Model Setup**

12 Put description of Fig. 1 in this section.

13 Don't forget to mention 1-2-1 smoother.

14 The numerical simulations were performed using version 19.4 of Cloud Model
15 1 (CM1) described in Bryan and Rotunno (2009) and available online at
16 <http://www2.mmm.ucar.edu/people/bryan/cm1/>. The fully-compressible equations of mo-
17 tion were integrated on a 3000-km-wide, 35-km-deep, axisymmetric grid with 1-km horizontal
18 and 250-m vertical grid spacing. Horizontal turbulence was parameterized using a Smagorinsky
19 scheme described in Bryan and Rotunno (2009, their Eq. 17), with a prescribed mixing length
20 that varied linearly from 100 m at a surface pressure of 1015 hPa to 1000 m at a surface pressure
21 of 900 hPa. This formulation allows for realistically-large horizontal mixing lengths near the
22 hurricane's inner core, consistent with the results of Bryan (2012), while not over-representing
23 horizontal turbulence in convection at outer radii. Vertical turbulence was parameterized using
24 the formulation of Markowski and Bryan (2016, their Eq. 6), using an asymptotic vertical
25 mixing length of 100 m. A Rayleigh damping layer was applied outside of the 2900-km radius
26 and above the 25-km level to prevent spurious gravity wave reflection at the model boundaries.
27 Microphysical processes were parameterized using the Thompson et al. (2004) microphysics
28 scheme and radiative heating tendencies were computed every two minutes using the RRTMG
29 longwave and shortwave schemes (Iacono et al. 2008). A horizontally-homogeneous temperature
30 and humidity field was initialized with a mean sounding computed using all dropsondes deployed
31 during the TCI flight conducted within and around Tropical Storm Patricia on 21 October, 2015

32 (see Doyle et al. 2017 for details.) Since relative humidity measurements were unreliable at
33 temperatures below -40°C Bell et al. (2016), the water vapor mixing ratio was assumed to be zero
34 above 16 km.

35 **3. Budget Computation**

36 Add details of budget computation here...

37 **4. Results**

38 *a. Static stability evolution*

39 The average N^2 over the first day of the simulation (Fig. 2a) indicates the presence of a static
40 stability maximum about 400 m above the cold-point tropopause. This lower-stratospheric stable
41 layer had begun to erode during the initial spin-up period, with the maximum destabilization
42 occurring at the innermost radii. This decrease in static stability continued into the second day
43 of the simulation (Fig. 2b) as the storm intensified to hurricane strength (Fig. 1). Destabilization
44 was particularly pronounced over the developing eye, where the time-mean cold-point tropopause
45 height increased by up to 400 m compared to the previous day. Over the developing eyewall
46 and outer rainband regions, meanwhile, the tropopause height remained nearly constant. During
47 the third day of the simulation (Fig. 2c), static stability over the eye continued to decrease, and
48 the cold-point tropopause height rose to 18.3 km at the storm center. The tropopause sloped
49 sharply downward over the innermost radii, reaching the 16.4-km level near the 50-km radius. This
50 local minimum in tropopause height corresponded to the eyewall region, where upper-tropospheric
51 static stability increased during this time period. Outside of the eyewall region, static stability
52 began to increase in the layer immediately overlying the cold-point tropopause. This stable layer
53 sloped upward with radius, which corresponded to an upward-sloping tropopause radially outside

54 of the eyewall region. Over the next 24 hours (Fig. 2d), as the storm's maximum 10-m wind
 55 speed leveled off near 80 m s^{-1} (Fig. 1), the upper-tropospheric static stability within the eyewall
 56 region continued to strengthen, as did the static stability just above the cold-point tropopause
 57 radially outside of the eyewall. As the stable layer strengthened, its altitude rose slightly, which
 58 corresponded to a slight increase in tropopause height outside of the eyewall during this period.
 59 Within the upper troposphere radially outside of the eyewall, meanwhile, static stability decreased
 60 such that it was nearly neutral in a thin layer between the 120- and 150-km radii. The eye region
 61 likewise continued to destabilize, and the cold-point tropopause height increased to a level above
 62 18.5 km. This static stability evolution closely follows that observed in Hurricane Patricia (2015;
 63 Duran and Molinari 2018).

64 *b. Static stability budget analysis*

65 The left column of Fig. 3 depicts 24-hour changes in N^2 over each of the four days of the
 66 simulation. These represent bulk changes computed by subtracting the instantaneous N^2 at the
 67 initial time from the instantaneous N^2 at the final time. The middle column of Fig. 3 represents
 68 the change in N^2 computed using Eq. XXX and the method described in Section 3. The residual
 69 between these two computations (Fig. 3, right column) is much smaller than the change in N^2 ,
 70 meaning that the budget performs well within the analysis domain.

71 To determine which of the budget terms are most important, a time series of the contribution of
 72 each of the budget terms in Eq. XXX to the tropopause-layer static stability tendency is plotted
 73 in Fig. 4. For this figure, each of the budget terms is computed using the method described in
 74 Section 3, except with 1-hour averaging intervals instead of 24-hour intervals. The absolute values
 75 of these tendencies are then averaged over the radius-height domain depicted in Fig. 3 and plotted

as a time series¹. Advection (Fig. 4, red line) plays an important role in the mean tropopause-layer static stability tendency at all times, and vertical turbulence (Fig. 4, blue line) and radiation (Fig. 4, dark green line) both become important after 48 hours. Although the contribution from horizontal turbulence (Fig. 4, purple line) becomes more important after 72 hours, it is confined to a very small region immediately surrounding the eyewall tangential velocity maximum (not shown), and is negligible throughout the rest of the tropopause layer. The remaining two processes - microphysics and dissipative heating (Fig. 4, orange and light green lines, respectively) - lie atop one another near zero. These time series indicate that, at all times, three budget terms dominate the tropopause-layer static stability tendency: advection, vertical turbulence, and radiation. Variations in the magnitude and spatial structure of these terms drive the static stability changes depicted in Fig. 2; subsequent sections will focus on these variations and what causes them.

(i) 0-24 hours The first 24 hours of the simulation was characterized by a weakening of the lower-stratospheric static stability maximum above 17 km (Fig. ??a, purple shading) and an increase in static stability below (green shading). Although these tendencies extended out to the 200-km radius, they were particularly pronounced at innermost radii. A comparison of the contributions of advection (Fig. ??b), vertical turbulence (Fig. ??c), and radiation (Fig. ??d) reveals that advection is primarily responsible for the change in static stability during this period. ...Explain this in the context of radial and vertical velocities...

(ii) 24-48 hours During the second day of the simulation, the lower-stratospheric stable layer continued to weaken (Fig. 6a). This weakening trend in the 16.75-17.75-km layer extended from the 50 km radius outward to past 200 km, and was primarily driven by advection (Fig. 6b). Below

¹It will be seen in subsequent figures that each of the terms contributes both positively and negatively to the N^2 tendency within the analysis domain. Thus, taking an average over the domain tends to wash out the positive and negative contributions. To circumvent this problem, the absolute value of each of the terms is averaged, yielding a time series of the mean magnitude of each budget term.

97 this layer, static stability began to increase slightly. This stabilization had contributions from both
98 vertical turbulence (Fig. 6c) and radiation (Fig. 6d) in the 16-16.5-km layer. ...Explain this in
99 context of mean vertical mixing coefficient and mean radiative heating tendency... Meanwhile,
100 radially inward of 60 km, static stability below 17.5 km continued to weaken, primarily due to
101 advective processes.

102 (iii) 48-72 hours The third day of the simulation marked a dramatic change in the structure of the
103 tropopause-layer static stability tendencies. During this time, static stability increased markedly
104 in an upward-sloping region within the 30-60-km radial band (Fig. 7a), and also increased within
105 the 16.75-17.5-km layer out to at least the 200-km radius. As this layer stabilized, the layer
106 immediately below it destabilized in a broad region extending from 60-200 km. Examination
107 of the contribution from total advection (Fig. 7b) reveals that advection no longer dominates the
108 static stability tendencies. Instead, a combination of vertical turbulence (Fig. 7c) and radiation
109 (Fig. 7d) overcomes the destabilizing influence of advection to create the layer of increasing static
110 stability. Meanwhile, the destabilizing influence of vertical turbulence in a broad region below
111 17 km combines with a small region of destabilization due to radiation in the 50-120-km radial
112 band combine to destabilize the layer below 16.5 km in the 50-200-km radial band. Comparing
113 the sum of advection and vertical turbulence (Fig. 7e) to the sum of advection, vertical turbulence,
114 and radiation (Fig. 7f) reveals that radiation plays a fundamental role in the re-strengthening of the
115 lower-stratospheric stable layer during this time.

116 (iv) 72-96 hours

117 *Acknowledgments.* Start acknowledgments here.

References

- Bell, M. M., and Coauthors, 2016: Office of Naval Research Tropical Cyclone Intensity (TCI) 2015 NASA WB-57 High Density Dropsonde Sounding System (HDSS) data, version 1.0. doi: 10.5065/D6KW5D8M.
- Bryan, G. H., 2012: Effects of surface exchange coefficients and turbulence length scales on the intensity and structure of numerically simulated hurricanes. *Mon. Wea. Rev.*, **140**, 1125–1143.
- Bryan, G. H., and R. Rotunno, 2009: The maximum intensity of tropical cyclones in axisymmetric numerical model simulations. *Mon. Wea. Rev.*, **137**, 1770–1789.
- Doyle, J. D., and Coauthors, 2017: A view of tropical cyclones from above: The Tropical Cyclone Intensity (TCI) Experiment. *Bull. Amer. Meteor. Soc.*, **98**, 2113–2134.
- Duran, P., and J. Molinari, 2018: Dramatic inner-core tropopause variability during the rapid intensification of Hurricane Patricia (2015). *Mon. Wea. Rev.*, **XXX**, XXX–XXX.
- Iacono, M. J., J. S. Delamere, E. J. Mlawer, M. W. Shephard, S. A. Clough, and W. D. Collins, 2008: Radiative forcing by long-lived greenhouse gases: Calculations with the AER radiative transfer models. *J. Geophys. Res.*, **113** (D13103).
- Markowski, P. M., and G. H. Bryan, 2016: LES of laminar flow in the PBL: A potential problem for convective storm simulations. *Mon. Wea. Rev.*, **144**, 1841–1850.
- Thompson, G., R. M. Rasmussen, and K. Manning, 2004: Explicit forecasts of winter precipitation using an improved bulk microphysics scheme. Part I: Description and sensitivity analysis. *Mon. Wea. Rev.*, **132**, 519–542.

LIST OF FIGURES

- Fig. 1.** The maximum 10-m wind speed (top panel; m s^{-2}) and minimum sea-level pressure (bottom panel; hPa) in the simulated storm (blue lines) and from Hurricane Patricia's best track (red stars). 11
- Fig. 2.** Twenty-four-hour averages of squared Brunt-Väisälä frequency (10^{-4} s^{-2}) over the first four days of the simulation. Orange lines represent the cold-point tropopause computed from the mean temperature field over the same time periods. 12
- Fig. 3.** Left panels: Twenty-four-hour changes in squared Brunt-Väisälä frequency (10^{-4} s^{-2}) over (a) 0-24 hours, (b) 24-48 hours, (c) 48-72 hours, (d) 72-96 hours. Middle Panels: The N^2 change over the same time periods computed using Eq. XXX. Right Panels: The budget residual over the same time periods, computed by subtracting the budget change (middle column) from the model change (left column). 13
- Fig. 4.** Time series of the contribution of each of the budget terms to the time tendency of the squared Brunt-Väisälä frequency (N^2 ; 10^{-4} s^{-2}). For each budget term, the absolute value of the N^2 tendency is averaged both temporally over 1-hour periods (using output every minute), and spatially within the radius-height domain depicted in Fig. 3. 14
- Fig. 5.** (a) Total change in N^2 over the 0-24-hour period ($10^{-4} \text{ s}^{-2} (24 \text{ hr})^{-1}$) and the contributions to that change from (b) the sum of horizontal and vertical advection, (c) vertical turbulence, and (d) the sum of longwave and shortwave radiation. 15
- Fig. 6.** As in Fig. 5, but for the 24-48-hour period. 16

158	Fig. 7.	(a) Total change in N^2 over the 48-72-hour period ($10^{-4} \text{ s}^{-2} (24 \text{ hr})^{-1}$) and the contributions	
159		to that change from (b) the sum of horizontal and vertical advection, (c) vertical turbulence,	
160		(d) the sum of longwave and shortwave radiation, (e) the sum of horizontal advection, ver-	
161		tical advection, and vertical turbulence, and (f) the sum of horizontal advection, vertical	
162		advection, vertical turbulence, and longwave and shortwave radiation.	17
163	Fig. 8.	As in Fig. 7, but for the 72-96-hour period.	18
164	Fig. 9.	Radial velocity (m s^{-1} ; filled contours), potential temperature (K; thick black contours), and	
165		cold point tropopause height (orange line) averaged over (a) 0-24 hours, (b) 24-48 hours, (c)	
166		48-72 hours, and (d) 72-96 hours.	19
167	Fig. 10.	Vertical velocity (cm s^{-1} ; filled contours), potential temperature (K; thick black contours),	
168		and cold point tropopause height (orange line) averaged over (a) 0-24 hours, (b) 24-48 hours,	
169		(c) 48-72 hours, and (d) 72-96 hours.	20
170	Fig. 11.	Total condensate mixing ratio (g kg^{-1}) and cold point tropopause height (orange line) aver-	
171		aged over (a) 0-24 hours, (b) 24-48 hours, (c) 48-72 hours, and (d) 72-96 hours.	21

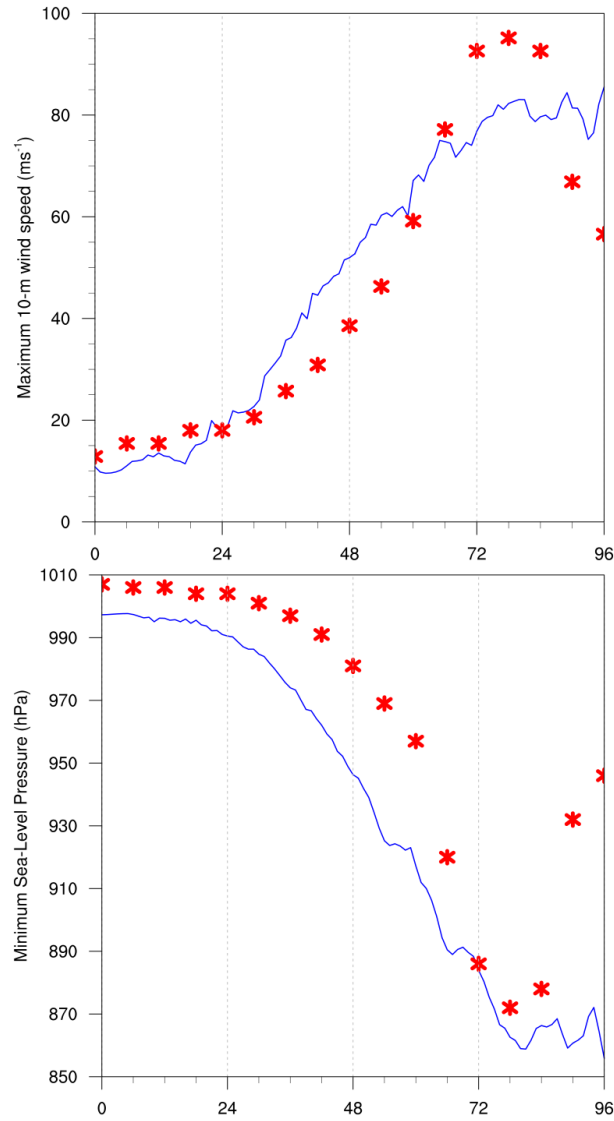


FIG. 1. The maximum 10-m wind speed (top panel; m s^{-2}) and minimum sea-level pressure (bottom panel; hPa) in the simulated storm (blue lines) and from Hurricane Patricia's best track (red stars).

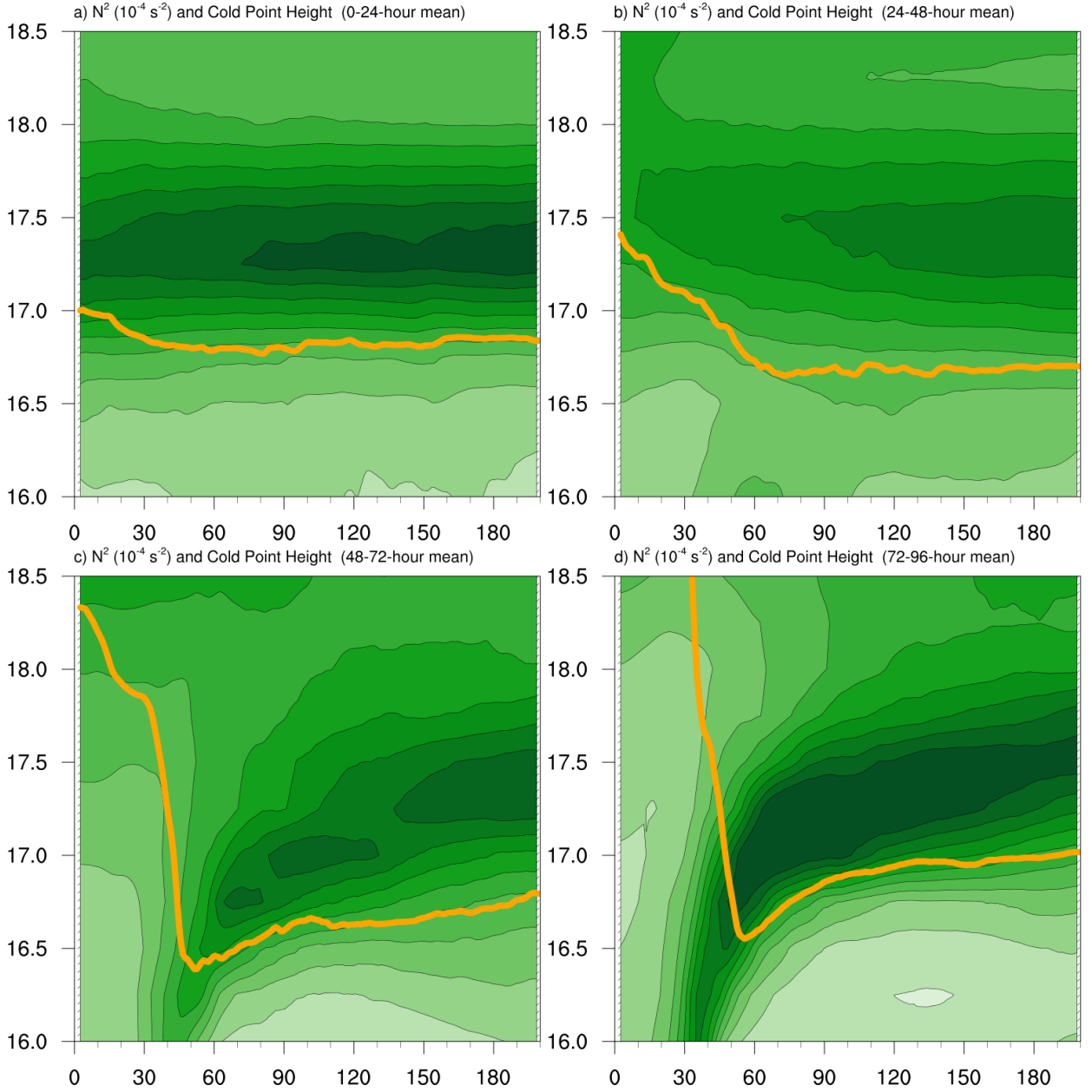
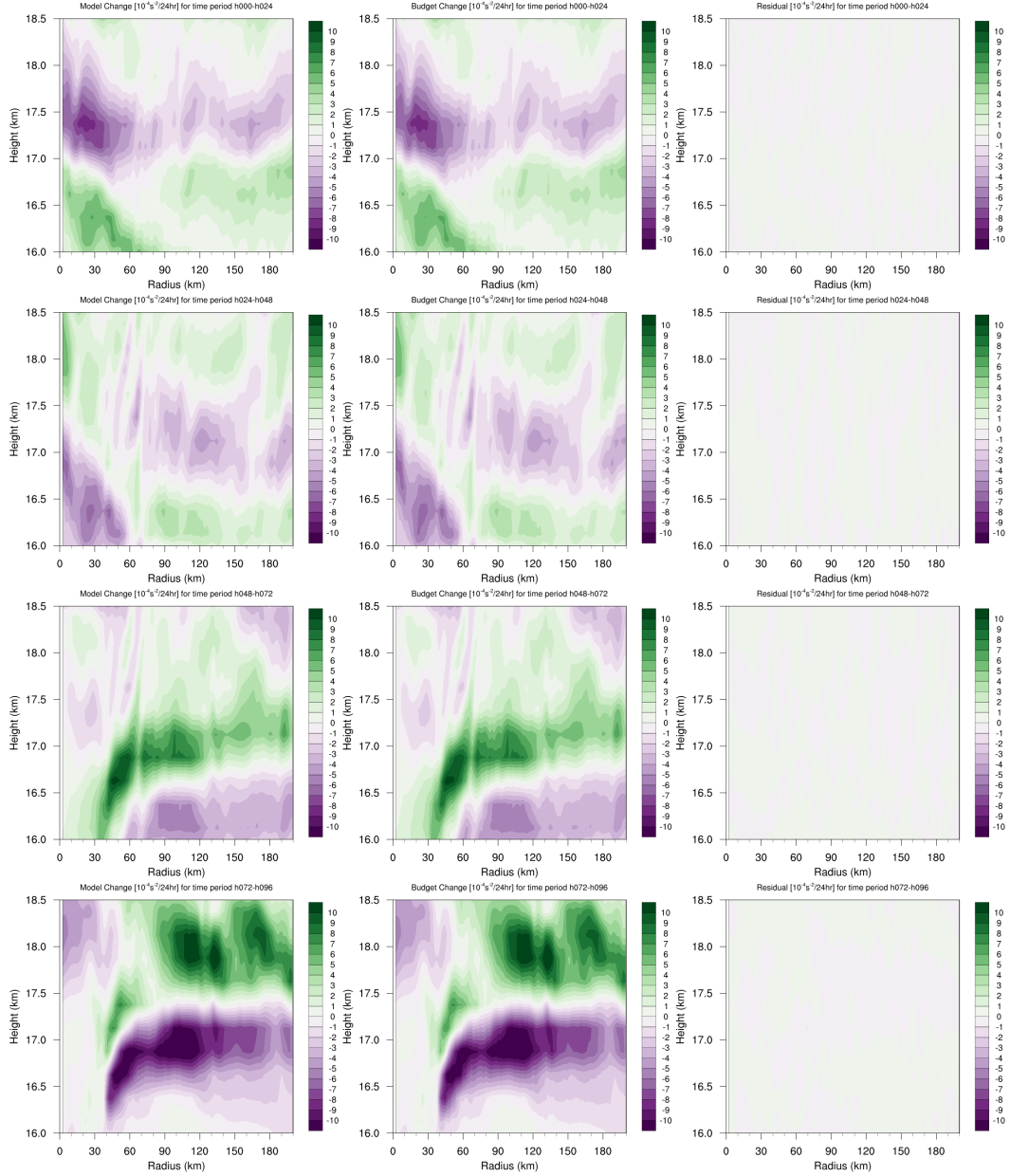
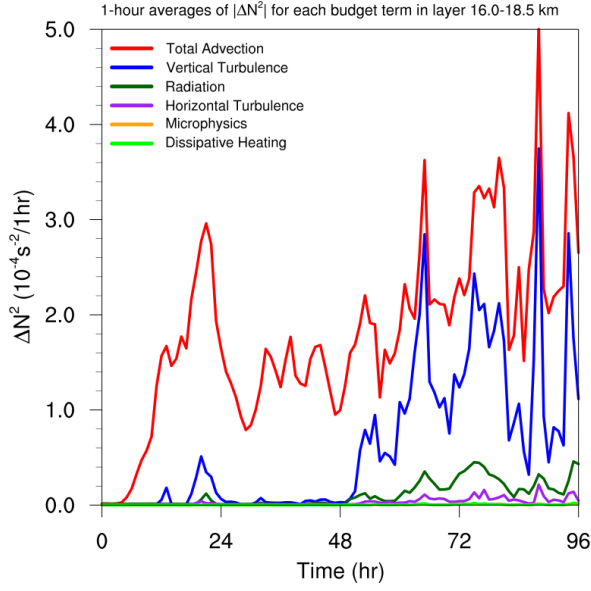


FIG. 2. Twenty-four-hour averages of squared Brunt-Väisälä frequency (10^{-4} s^{-2}) over the first four days of the simulation. Orange lines represent the cold-point tropopause computed from the mean temperature field over the same time periods.



177 FIG. 3. Left panels: Twenty-four-hour changes in squared Brunt-Väisälä frequency (10^{-4} s^{-2}) over (a) 0-24
 178 hours, (b) 24-48 hours, (c) 48-72 hours, (d) 72-96 hours. Middle Panels: The N^2 change over the same time
 179 periods computed using Eq. XXX. Right Panels: The budget residual over the same time periods, computed by
 180 subtracting the budget change (middle column) from the model change (left column).



181 FIG. 4. Time series of the contribution of each of the budget terms to the time tendency of the squared
 182 Brunt-Väisälä frequency (N^2 ; 10^{-4} s^{-2}). For each budget term, the absolute value of the N^2 tendency is averaged
 183 both temporally over 1-hour periods (using output every minute), and spatially within the radius-height domain
 184 depicted in Fig. 3.

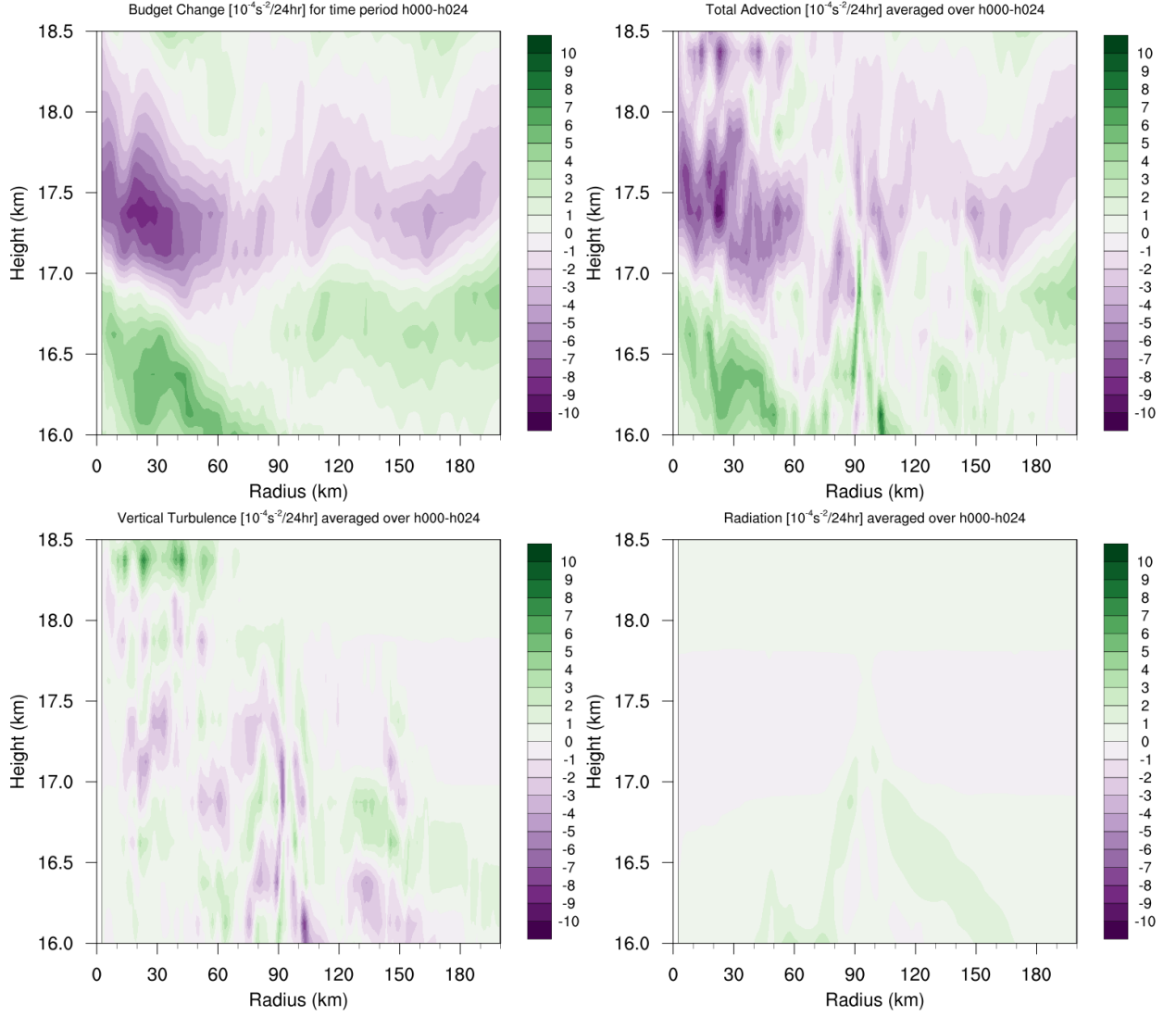


FIG. 5. (a) Total change in N^2 over the 0-24-hour period ($10^{-4} \text{ s}^{-2} (24 \text{ hr})^{-1}$) and the contributions to that change from (b) the sum of horizontal and vertical advection, (c) vertical turbulence, and (d) the sum of longwave and shortwave radiation.

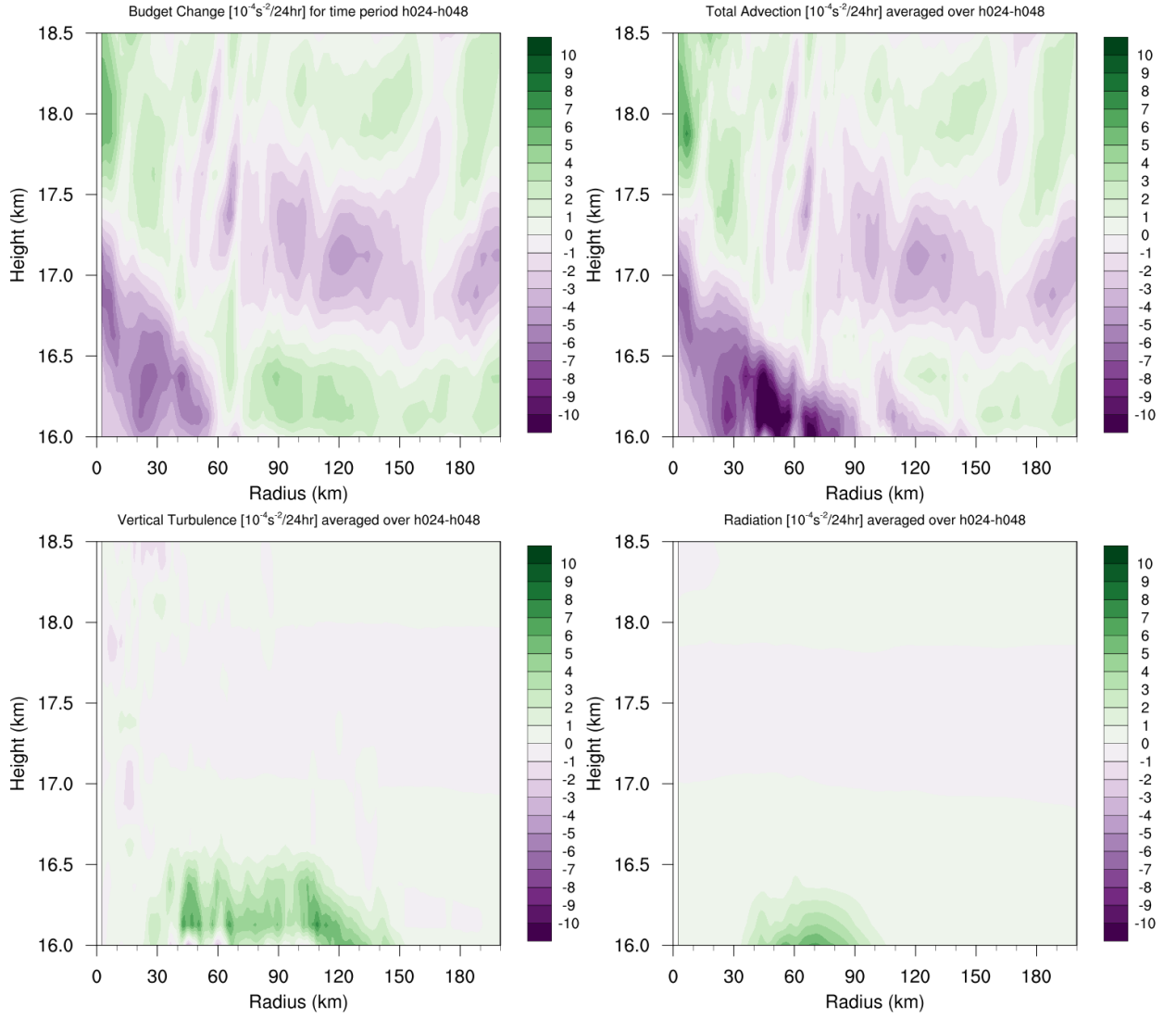


FIG. 6. As in Fig. 5, but for the 24-48-hour period.

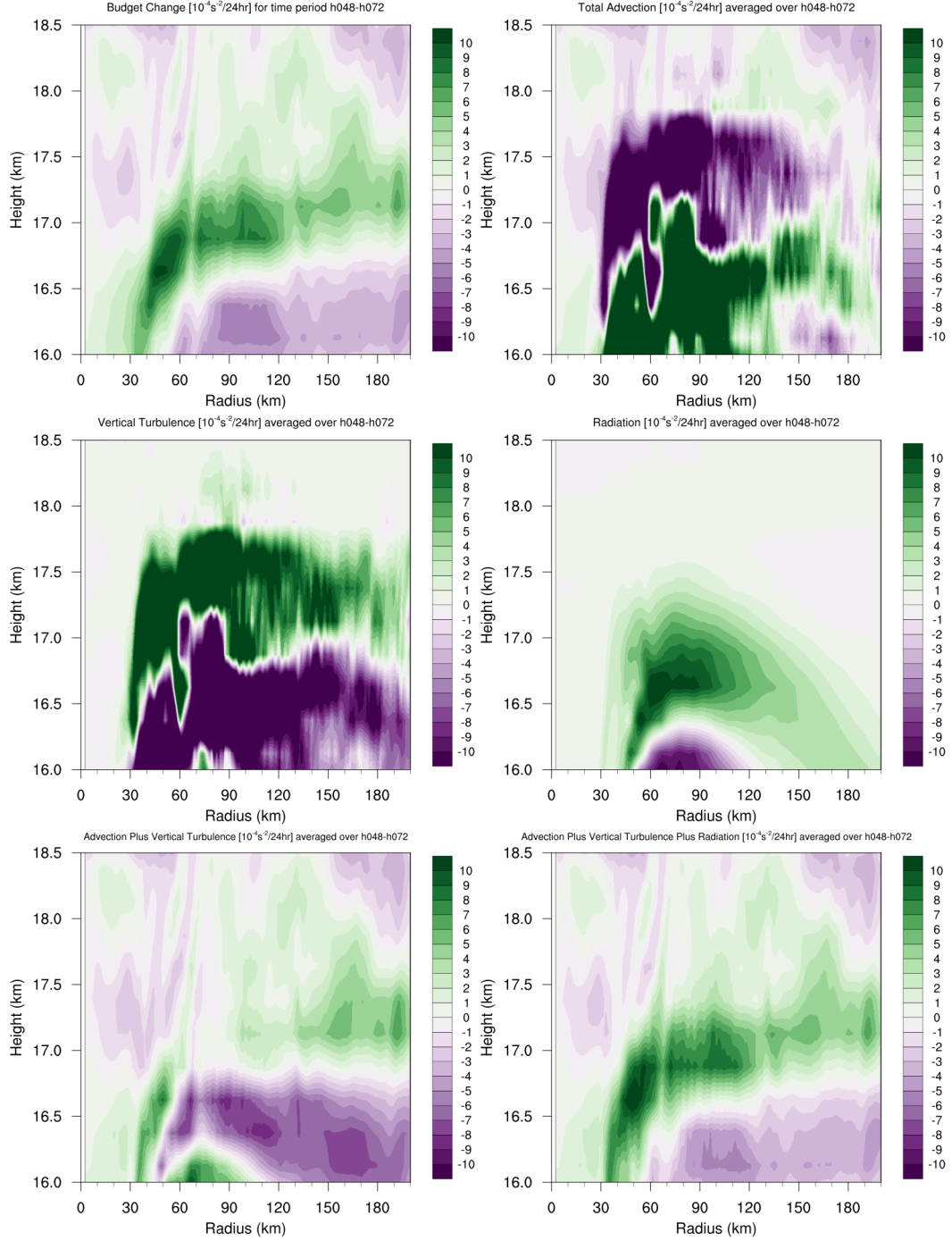


FIG. 7. (a) Total change in N^2 over the 48-72-hour period ($10^{-4} \text{ s}^{-2} (24 \text{ hr})^{-1}$) and the contributions to that change from (b) the sum of horizontal and vertical advection, (c) vertical turbulence, (d) the sum of longwave and shortwave radiation, (e) the sum of horizontal advection, vertical advection, and vertical turbulence, and (f) the sum of horizontal advection, vertical advection, vertical turbulence, and longwave and shortwave radiation.

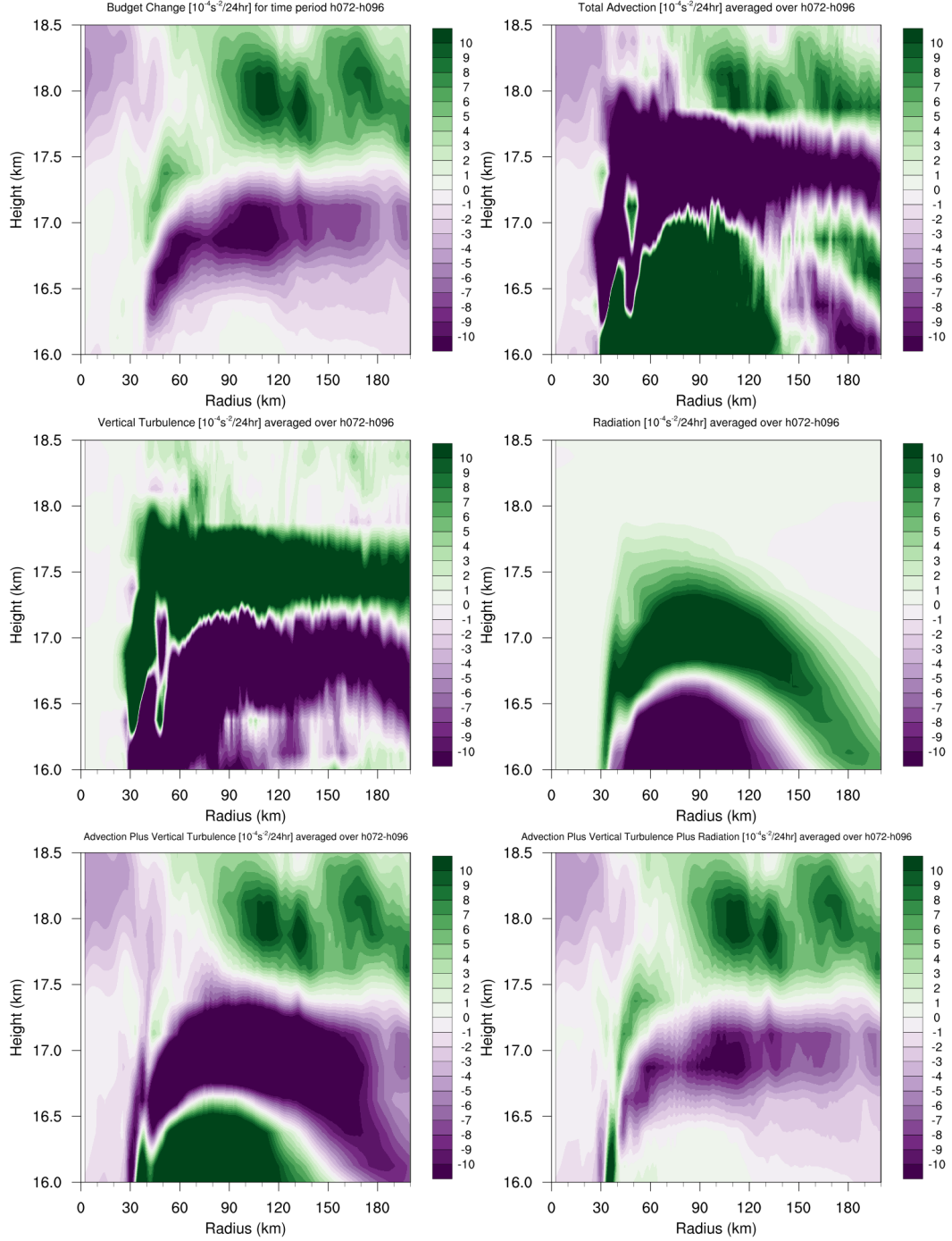


FIG. 8. As in Fig. 7, but for the 72-96-hour period.

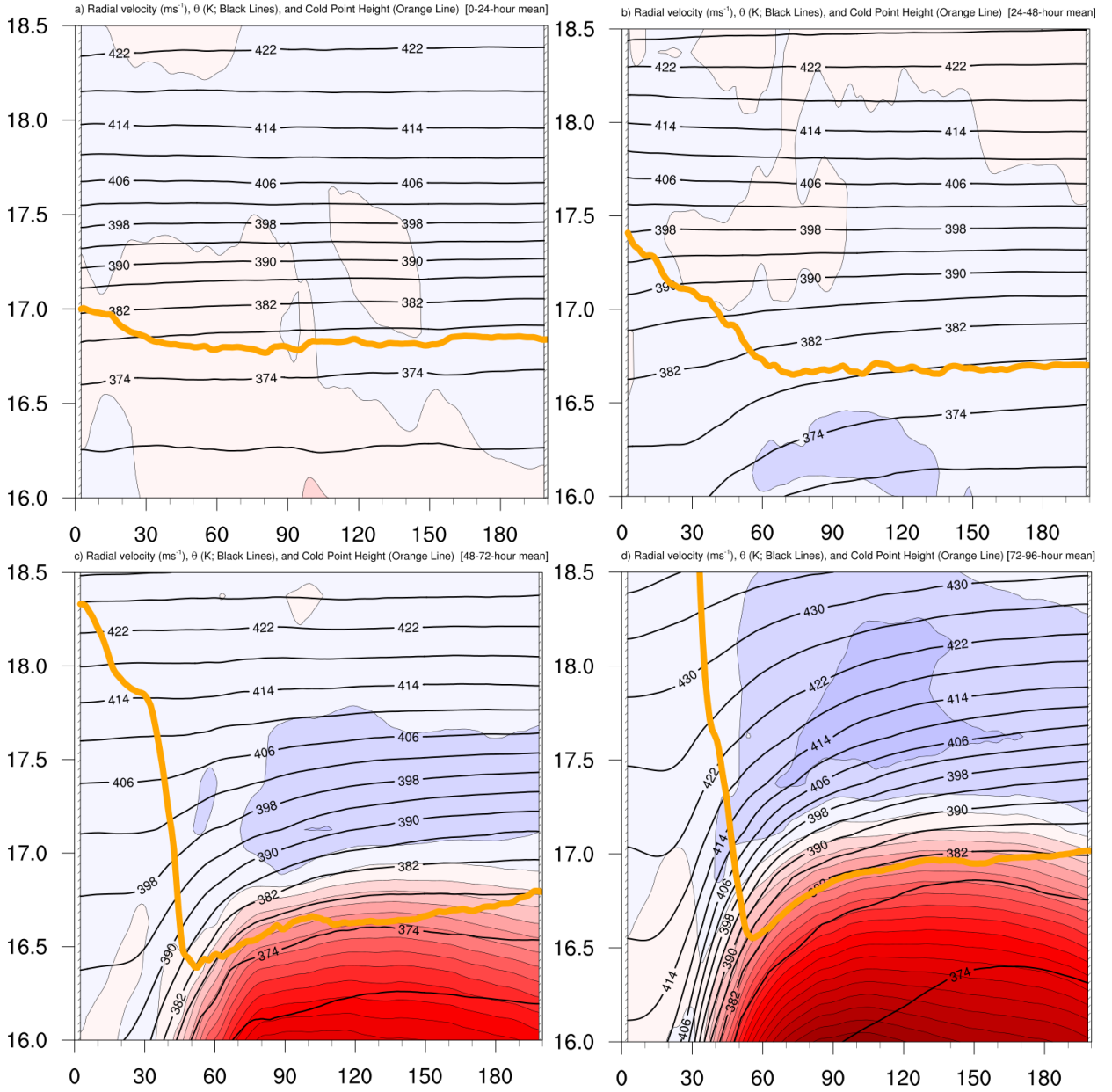


FIG. 9. Radial velocity (m s^{-1} ; filled contours), potential temperature (K; thick black contours), and cold point tropopause height (orange line) averaged over (a) 0-24 hours, (b) 24-48 hours, (c) 48-72 hours, and (d) 72-96 hours.

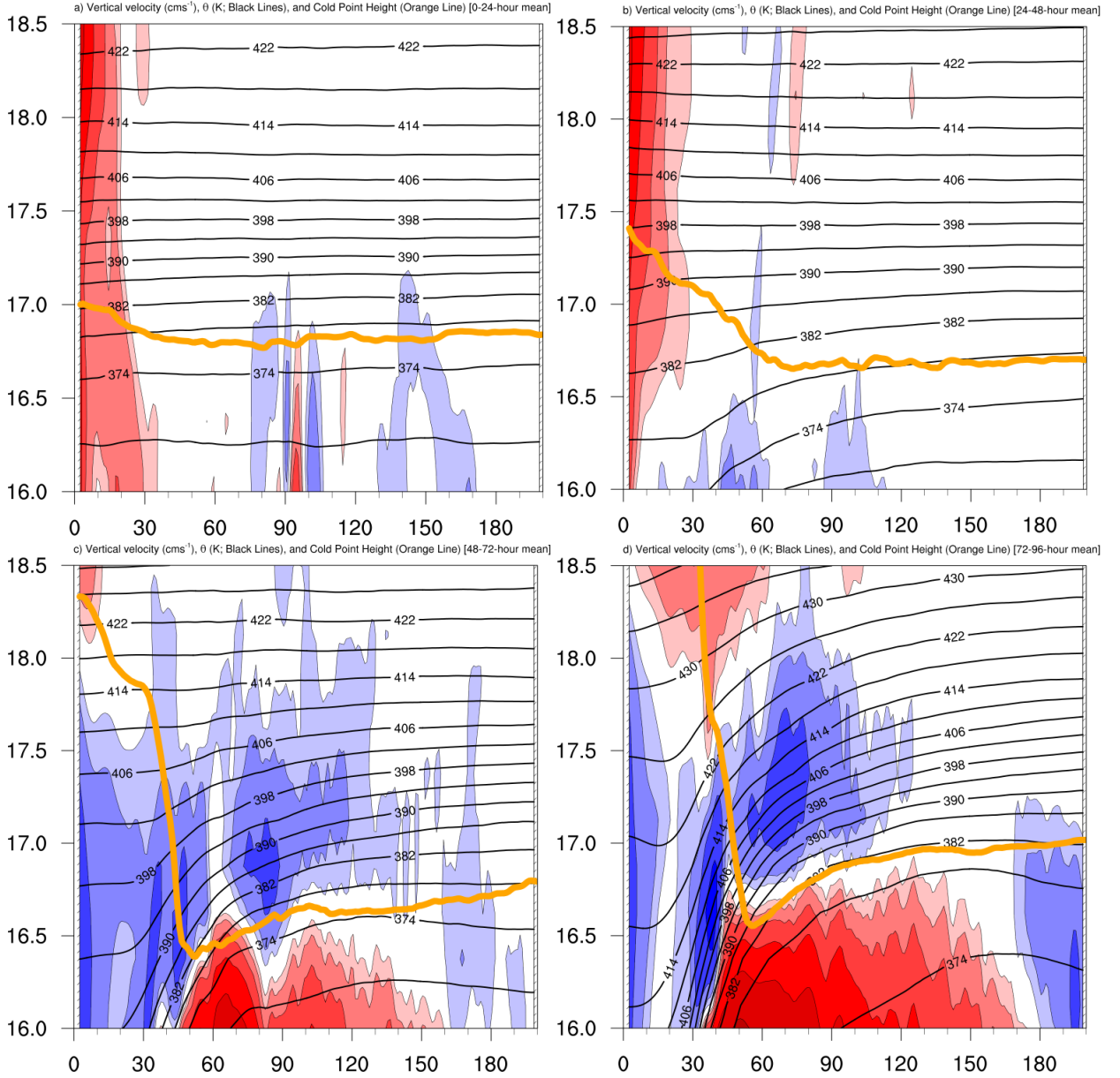


FIG. 10. Vertical velocity (cm s^{-1} ; filled contours), potential temperature (K ; thick black contours), and cold point tropopause height (orange line) averaged over (a) 0-24 hours, (b) 24-48 hours, (c) 48-72 hours, and (d) 72-96 hours.

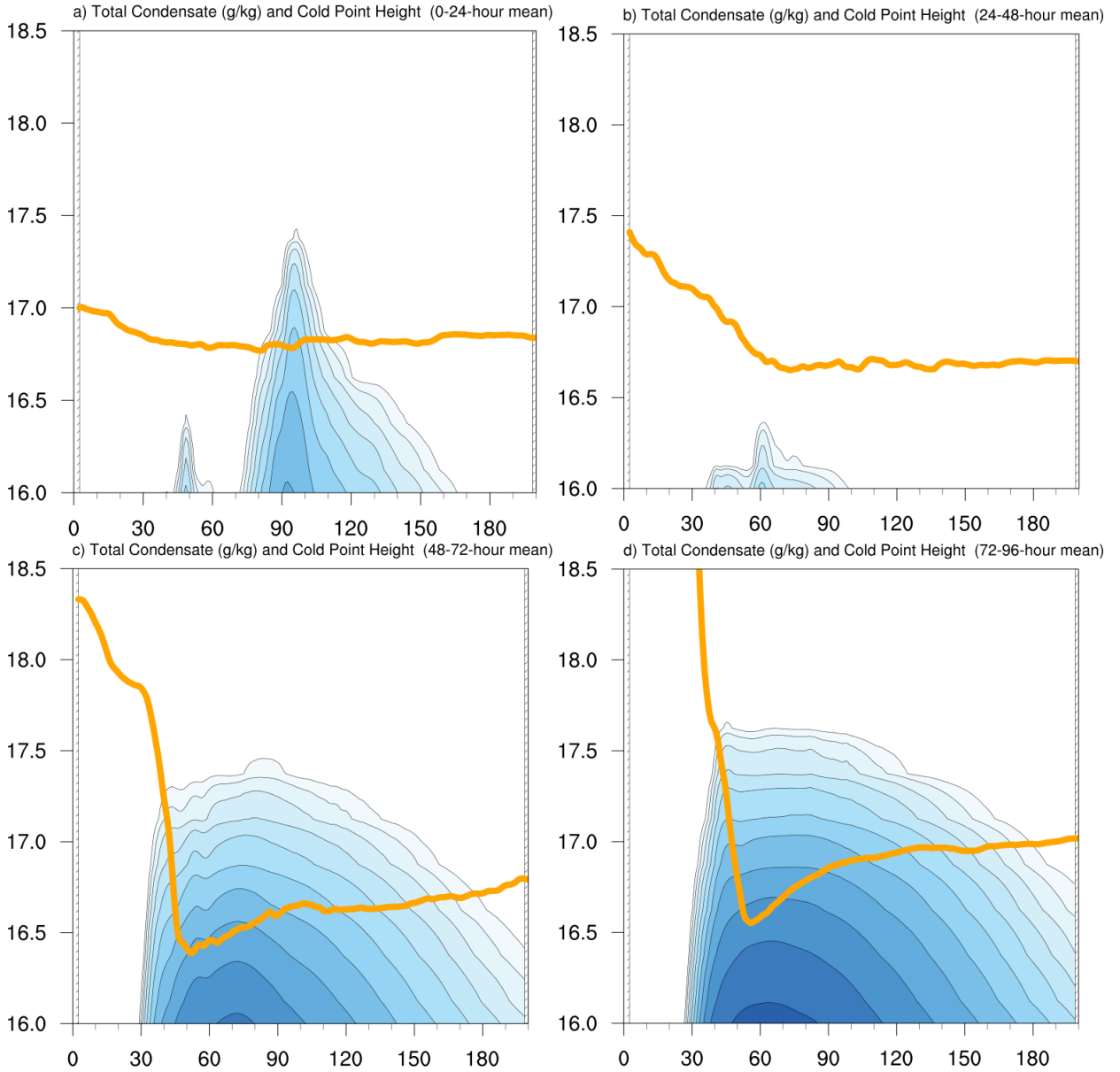


FIG. 11. Total condensate mixing ratio (g kg^{-1}) and cold point tropopause height (orange line) averaged over
(a) 0-24 hours, (b) 24-48 hours, (c) 48-72 hours, and (d) 72-96 hours.